Journal of Alloys and Compounds 840 (2020) 155648

Contents lists available at ScienceDirect

Journal of Alloys and Compounds

journal homepage: http://www.elsevier.com/locate/jalcom

Structural characterization and nanoindentation studies on mechanical properties of spark plasma sintered duplex stainless steel nanocomposite

Samuel Ranti Oke [a, b, *], Mahlatse R. Mphahlele [c], Oladeji Oluremi Ige [c, d], Oluwasegun Eso Falodun [c], Avwerosuoghene Moses Okoro [c], Peter Apata Olubambi [c]

[a] Department for Management of Science and Technology Development, Ton Duc Thang University, Ho Chi Minh City, Viet Nam
[b] Faculty of Civil Engineering, Ton Duc Thang University, Ho Chi Minh City, Viet Nam
[c] Centre for Nanoengineering and Tribocorrosion, School of Mining, Metallurgy and Chemical Engineering, University of Johannesburg, Johannesburg, South Africa
[d] Department of Materials Science and Engineering, Obafemi Awolowo University, Ile-Ife, Osun State, Nigeria

ARTICLE INFO

Article history:
Received 13 December 2019
Received in revised form
13 May 2020
Accepted 14 May 2020
Available online 26 May 2020

Keywords:
Spark plasma sintering (SPS)
Duplex stainless steel (SAF 2205)
Titanium nitride (TiN)
Nanoindentation
Interfacial characterization

ABSTRACT

Nano-sized titanium nitride (TiN) powders were used as reinforcements for the fabrication of duplex stainless steel (SAF 2205) via spark plasma sintering (SPS) route. Optimized parameters of 1150 °C temperature, 100 °C/min heating rate, 50 MPa pressure and 15 min holding time were utilized for sintering of the SAF 2205-TiN composite. SEM equipped with an EBSD and TKD detectors were used to gain insight into sintered composite microstructures and grain boundary character. XRD was used to study crystallinity and phase transformation. The discrete mechanical properties of ferrite/austenite grains and grain boundaries were studied using nanoindentation technique. The addition of TiN nanoparticles resulted in decrease of the α-Fe peaks with principal planes shifting from α-Fe (110) to γ-Fe (111). The EBSD confirmed that the addition of TiN nanoparticles to duplex stainless steel could initiate and advance ferrite to austenite phase reverse transformation. The TKD confirmed that nanosized nitrides are concentrated at the ferrite/austenite interface. The nanoindentation studies showed that the nanohardness (H), elastic modulus (E), plasticity index (Ψ), and anti-wear properties were improved with the TiN nanoparticle addition from 0 to 8 wt%.

1. Introduction

The processing method adopted in materials synthesis have a strong impact on the structure and resulting mechanical properties of the material [1,2]. The fabrication of stainless steels by powder metallurgy route is on the increase due to their applications in industries including aerospace, automobile, recreational, biomedical and chemical processing [3,4]. Metallurgically sintered stainless steels have comparable advantages of low porosity levels over cast steels [4]. Another landmark in producing stainless steels by powder metallurgy is that the properties can be easily manipulated by dispersion of the second phase particles into the steel's matrix [5,6]. The objective of adding second phase particles is to refine its microstructure and enhance sintered stainless steel applications which are restricted by its susceptibility to galling and wear [7,8]. Although numerous powder metallurgy techniques are in operation, the motivation is to have products with good densification and mechanical properties.

In this work, duplex stainless steel (SAF 2205) reinforced with second phase nanoparticles of titanium nitride (TiN) was fabricated through spark plasma sintering (SPS). The SPS is of interest due to its versatility and advantages of high material performance, high energy efficiency, short operating time because it uses high electric current densities over conventional sintering techniques [9–12]. The addition of secondary particles is well known to improve materials performance in service. However, there is no agreement on the mode of the strengthening mechanism [13]. This has led to debate over whether or not a nanostructured grain size is beneficial. Regardless of the benefits, it is evident that a significant higher number of atoms resides along grain boundaries in nanostructured

---

* Corresponding author. Ton Duc Thang University, Ho Chi Minh City, Viet Nam.
E-mail address: samuel.ranti.oke@tdtu.edu.vn (S.R. Oke).

https://doi.org/10.1016/j.jallcom.2020.155648

materials. The knowledge of the grain boundaries effect on the overall mechanical properties is essential to the development of bulk nanostructured composites [14].

Grain boundaries play a crucial role in controlling the mechanical properties of polycrystalline metals and composites [15,16]. Also, it is stated that the influence of grain boundaries on plastic deformation is not yet known, and there is no agreed physics-based model up till now. Studies have been done to resolve the critical role played by grain boundaries on materials behaviour [15,17]. The consensus is that there is no standardized measuring technique and procedure for such high precision materials response [15]. These prompt researchers to utilize nano and micro-indentation testing [18].

Nanoscale deformation of different materials have been studied using nanoindentation technique. Nanoindentation testing has some distinct features which include small materials volumes, sample cost-effectiveness, and higher speed [19,20]. Various studies have reported the use of nanoindentation to study plasticity, creep, fracture behaviour, crack growth, elastic modulus and hardness [21–23]. Most significantly, nanoindentation techniques provides the advantage of understanding plastic deformation and elastic-plastic transition regime of discrete phases within a microstructure. Efforts are continuously made to develop protocols that can convert raw indentation data to excellent mechanical properties [24,25]. This work adopted the approach of analysing indentation load-displacement data. It involves using the curvature in unloading data, the indentation depth, and the indenter shape.

Though preliminary investigations on the densification and microstructural changes that occur during spark plasma sintering of TiN nanoparticle dispersion strengthened SAF 2205 alloy using EBSD and TKD techniques have been reported in our previous work [26]. This study further gives details on the microstructure and elastic-plastic deformation behaviour of ferrite/austenite grains and grain boundaries of spark plasma sintered duplex stainless steel reinforced with different wt% of TiN nanoparticles. The aim is to gain insight into discrete nanoscale deformation phenomena and establish a relationship pathway between microstructure and mechanical properties. It is an experimental observation that utilizes nanoindentation technique to predict the plasticity index and wear behaviour of the sintered composite using strain-to-break and plastic deformation parameters.

2. Processing, Characterizations and Testing

The matrix material utilized for this work is SAF 2205 duplex stainless steel powders with chemical composition; C-$\leq$0.03, Si-$\leq$1.0, Mn-$\leq$2.0, P-$\leq$0.03, S-$\leq$0.015, Cr-22, Ni-5, Mo-3.2, N-0.18, Fe-bal wt.%. The matrix is reinforced with 20 nm sized TiN nanoparticles with chemical composition; C-0.03, Si-<0.003, Ni-5, N-<21.91, Ti-77.83, Fe-<0.001 wt %. The stainless steel powders with varying addition of TiN nanoparticles ranging from 0 to 8 wt% were homogeneously blended using a turbula mixer (T2F) for 6 h at 72 rpm. The mixed powders were poured into a 25 mm die and punches assembly lined with graphite paper to avoid contamination and ensure easy removal. The die and punch assembly containing the mixed powders was placed in the sintering chamber of an automated spark plasma sintering machine (model HHPD-25, FCT GmbH Germany) and consolidated using the following sintering parameters; 1150 °C sintering temperature, 100 °C/min heating rate, 50 MPa pressure and 15 min holding time. The selected SPS parameters is based on optimization results from our previous studies [27,28]. All experiments were performed under vacuum atmosphere. The sintered samples were sand blasted to remove the graphite contaminations on the outer surface or in the surface pores of the samples.

The analysis and evolution of phases was achieved with X-Ray diffractometry (XRD, PANalytical EMPYREAN) using Cu Kα radiation. Peak intensity analysis of the integrated areas for α-Fe and γ-Fe diffraction peaks in the XRD patterns were evaluated. Based on peak intensity ratios, the extent of α-Fe and γ-Fe phase transformation was predicted. To examine the ferrite and austenite phases, the sintered samples were cross sectioned and the surface were metallographically prepared following standard procedures. A JEOL 7001 F scanning electron microscope (SEM) equipped an electron backscatter diffraction (EBSD) detector was used to gain insight into sintered composite microstructures. To study the grain boundary interaction, the transmission kikuchi diffraction (TKD) analysis was conducted by horizontally mounting an approximately 60 nm thin foil samples in a JEOL JSM 7001F SEM equipped with a Nordlys-nano EBSD detector. The thin foil samples were prepared and cleaned using a Gatan Precision Ion Polishing System (PIPS) ion mill, equipped with a cold stage, to ensure a relatively large electron transparent area. Measurement of the foil thickness was achieved using focused ion beam scanning electron microscope. In order to obtain Kikuchi patterns, the system was set to operate at an acceleration voltage of 30 kV. The TKD analysis was achieved at a tilting angle of 20°, working distance was kept at 3.5 mm, and a hit rate was set to 91%. The overall speed of acquisition was 177.24 Hz.

The mechanical properties of the sintered duplex stainless steel were assessed using nanoindentation techniques. The experiment was conducted using an ultra nanoindenter (UNHT) facility equipped with Berkovich-shaped diamond indenter. Prior to indenting the test samples, the equipment was calibrated in accordance with ISO 14577 [25] standard using a fused silica of known properties. The equipment has a piezostage option which allows indentation at precise positions within the composite microstructure. It therefore became possible to perform indentation on different phases. A maximum load of 1 mN was used to make indents in two different regions: (i) ferrite/austenite phase (ii) interface-like region. The indenter was held at maximum load for 10 s to annihilate probable creep interference. To avoid errors due to the effect of thermal drift, the allowable drift rate is maintained at 0.08 nm/s. The indentation force-displacement curves are recorded as the indenter tip is pressed into the sample's surface and the indentation nanohardness and elastic modulus are obtained.

3. Results and Discussion

3.1. Crystallinity and ferrite to austenite phase balance with TiN addition

The surface crystallinity of the SPSed duplex stainless steel without TiN reinforcement was examined and compared with the diffraction pattern of the steel containing different percentages of TiN nanoparticles ranging from 2 to 8 wt%. The XRD in Fig. 1 revealed that irrespective of the TiN nanoparticle addition, the 0–8 wt% TiN stainless steel grades exhibited diffraction peaks with discrete reflections of α-Fe Phase (110), (200) (211) at 45.2°, 64.8° and 83.6° diffraction angles and γ-Fe phase (111), (200), (220) at 44.6°, and 50.8°, 74.1° and 83.6° Bragg's diffraction angles, respectively. The diffraction patterns of the sintered steel without TiN presented the ferrite as a dominant phase with α-Fe (110) nearing 6000 cps. The addition of TiN nanoparticles is however noted to have significant effect on the stability of the α-Fe phase. The XRD patterns depicting steel grades containing 2 to 8 wt% TiN are characterized by a less distinct and suppressed α-Fe phase with principal planes shifting from α-Fe (110) to γ-Fe (111). The reduction in peak intensity of the α-Fe phase intensified with continued addition of TiN up to 8 wt%. It is therefore

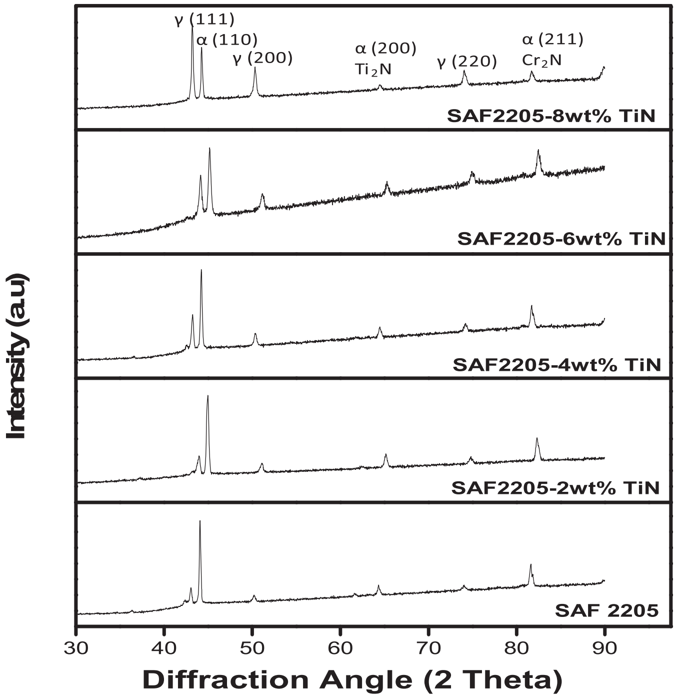

Fig. 1. X-ray diffraction pattern showing peaks corresponding to α-Fe and α-Fe with the evolution of Cr_2N and Ti_2N phases of the spark plasma sintered duplex stainless steel doped with different wt% of TiN.

suggested that addition of TiN nanoparticles to duplex stainless steel could initiate and advance ferrite to austenite phase reverse transformation. The α-Fe to γ-Fe phase transformation principally occurred during spark plasma sintering as a result of nitrogen diffusion from the TiN due to high sintering temperature. Nitrogen been a strong austenite stabilizer tends to suppress the formation of α-Fe [29]. At higher temperatures, the α-Fe is thermodynamic unstable and the solubility of nitrogen in α-Fe decreased. This causes the diffused nitrogen to occupy the interstice of the α-Fe crystallites and creating a mismatch strain that induces α-ferrite to γ-austenite transformation [11,26]. To intensify the discussion on the extent of transformation from α-Fe to γ-Fe, the peak intensity ratios are calculated and presented in Table 1. The peak intensity ratios are evaluated with reference to the principal crystal plane for each grade of sintered composite. It is confirmed from the table that dispersing nanoparticles of TiN increased the propensity of formation of γ-Fe while the α-Fe decreased progressively.

The EBSD was used to quantify the α-Fe and γ -Fe phases. The as obtained Phase fraction data from EBSD analysis of the stainless steel reinforced with 0 and 4 wt% TiN is presented in Table 2 while the phase, Euler and Inverse pole Figure (IPF) maps are presented in Fig. 2. The EBSD of the duplex steel containing 0 and 4 wt% TiN nanoparticles (Fig. 2; S0 and S4) revealed both BCC α-Fe (red colour) and FCC γ-Fe (blue colour) in the microstructure. The characteristic nearly equal amount of γ -Fe and α-Fe and of duplex stainless steels are observed in the SAF 2205 with no TiN nanoparticle addition (54.27 and 45.13% respectively). For the duplex stainless steel grades reinforced with 4 %wt of TiN, there is reduction in volume fraction of the α-Fe phase from 45.13 to 27.39%. The FCC γ-Fe is however noted to be dominant in the 4 wt% TiN steel with increase from 54.27 to 68.59%. The increase in γ-Fe phase affirmed the α-Fe to γ -Fe phase transformation earlier explained. The IPF map color code was used to identify the crystallographic orientations of the samples on a standard stereographic projection (green colour, [101]; red colour, [001]; and blue colour, [111]). The IPF maps indicated that the grains present in the sintered samples (S0 and S4) were randomly oriented rather than in a particular direction. This suggests uniform plastic deformation of admixed powders during sintering of the samples. The Euler maps revealed higher angle grain boundaries in the unreinforced stainless steel (S0) compared to the steel reinforced with 4 wt% (S4). The lower angle grain boundaries in S4 results in finer grain sizes of γ -Fe and α-Fe grains.

The XRD results (Fig. 1) revealed the precipitation of nitrides phases of Ti2N and Cr2N. The diffraction peaks of the nitride phases were detected in addition to the diffraction peaks of ferrite due to small amounts of nitrides formed. It has been reported that the preferential site for formation of nitride phases are at the grain boundaries [30]. However, the limited spatial resolution of the EBSD technique renders it an ineffective characterization tool for nanoparticle reinforced stainless steel. It therefore became imperative to analyse the interface of the austenite/ferrite phases using TKD. The observed TKD map of the duplex stainless steel reinforced with 4 wt% TiN is depicted in Fig. 3a. The location and nature of the evolved nitrides are revealed in the magnified TKD map. The ferrite/austenite interface confirmed that the yellow coloured nanosized nitrides are concentrated at the grain boundary and coexisted with ferrite and austenite. The reinforcing TiN was not observed within the ferrite/austenite grains but there was diffusion of nitrogen from the TiN to the duplex steel matrix. This assisted the transformation of ferrite to austenite. However, due to limited solubility of nitrogen in duplex steel and the fast cooling associated with SPS, sintered-in nitrides are trapped at the ferrite/austenite grain boundaries. Again, the variance in conductivity between the starting stainless steel and TiN powders during sintering could be responsible for nitride segregation at grain boundary [11]. The IPF and Euler maps revealed the crystallographic orientation of the grain boundary (Fig. 3b). The ferrite, austenite and TiN have the same specific crystallographic planes along the same specific crystallographic directions.

Information on the elemental segregation along the ferrite/austenite interface are revealed using the TKD-EDS. Fe, Cr, Ni, Mn and Ti are distinguished with the austenite and ferrite phases corresponding to a Ni and Cr-rich chemistries, respectively. Though nitrogen could not be detected in the TKD-EDS, the EDS compositional mapping presented a Ti and Mn rich grain boundary. The Ti and Mn rich phase as observed in the EDS was hardly indexed by

Table 1
The calculated peak intensity ratios with reference to the principal crystal plane for each grade of SAF 2205-TiN composite.

Series	Composite grades	Peak intensity ratio (I/Imax)					
		α-110	γ-111	γ −200	α −200	γ-220	α −211
S0	SAF 2205	100.0	23.4	11.4	16.2	10.9	31.2
S2	SAF 2205 + 2 wt% TiN	100.0	26.9	15.2	21.0	13.6	31.7
S4	SAF 2205 + 4 wt% TiN	100.0	48.0	19.7	17.0	14.9	31.2
S6	SAF 2205 + 6 wt% TiN	100.0	67.6	32.4	21.5	20.4	26.7
S8	SAF 2205 + 8 wt% TiN	70.2	100.0	41.6	10.6	23.3	17.6

Table 2
Phase fraction data of ferrite (α-Fe) and austenite (γ -Fe) obtained from EBSD Analysis for SAF 2205 reinforced with 0 and 4 wt% TiN.

Phase Name	Phase Fraction (%)	Phase Count	Mean Band Contrast	Standard Deviation Band Contrast	Phase Fraction (%)	Phase Count	Mean Band Contrast	Standard Deviation Band Contrast
	SAF 2205 without TiN (S0)				SAF 2205 with 4 wt% TiN (S4)			
α-Fe (BCC)	45.13	508084	170.34	12.13	27.39	308037	161.08	18.15
γ -Fe (FCC)	54.27	610988	177.74	13.46	68.59	771349	171.50	18.25
Zero Solutions	0.60	6703	122.93	30.72	4.02	45164	98.00	23.94

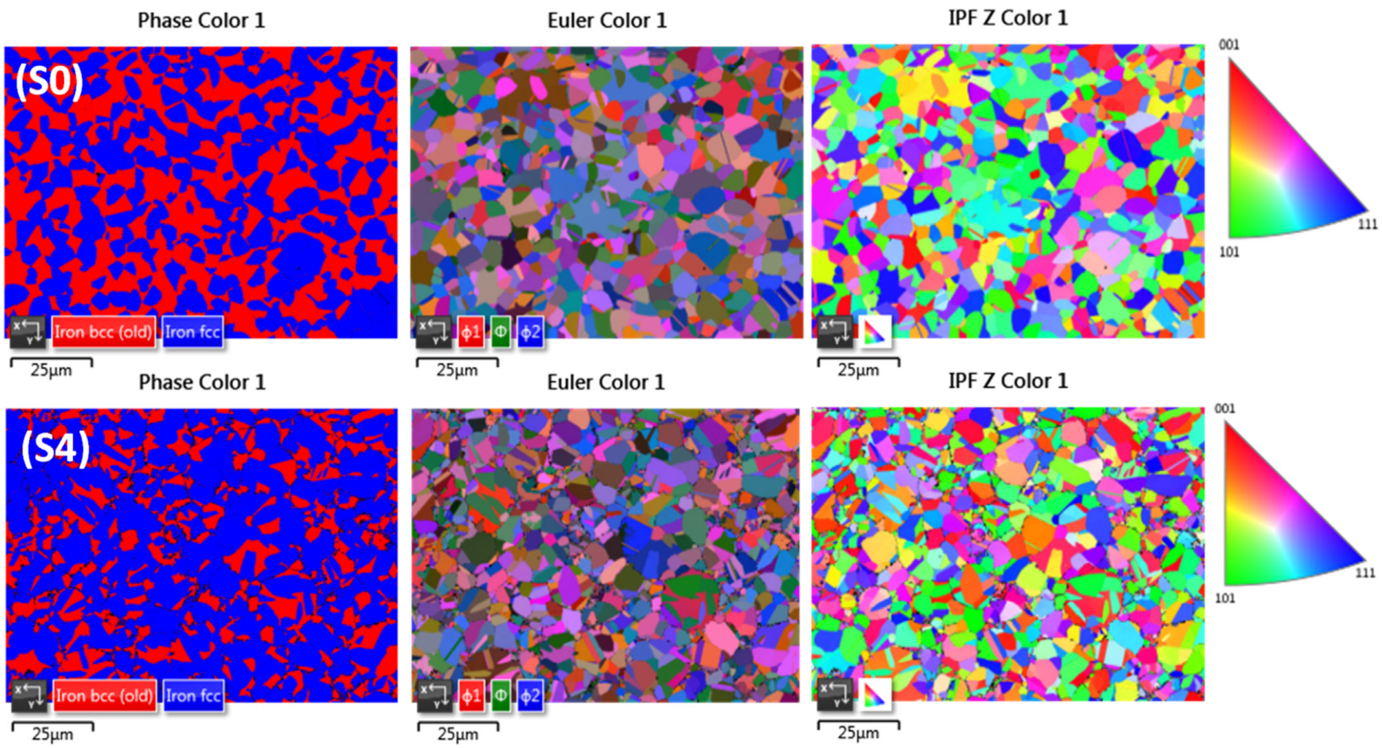

Fig. 2. EBSD phase maps with Euler and IPF of SAF 2205 reinforced with 0 and 4 wt% (S0 and S4) TiN nanoparticles. The ferrite (α-Fe) and austenite (γ -Fe) phases are identified as red and blue respectively. (For interpretation of the references to colour in this figure legend, the reader is referred to the Web version of this article.)

TKD due to non-indexed points that results when the data of the Kikuchi pattern cannot be indexed. attributed to voids present in the interaction volume of the electron beam during the TKD measurement.

3.2. Nanoindentation studies of mechanical properties of grain and grain boundary

3.2.1. Load-displacement curve of SAF 2205-TiN nanocomposite

The load displacements curves were obtained by performing a minimum of 10 indents on each of the composite grades. Substantial distance between each indent is ensured to avoid interactions and possible overlap of indentations. Indentations were performed separately on i) ferrite or austenite grains; and ii) nitride dominated ferrite/austenite interface. Characteristic indentation profile and resulting load–displacement curve during loading and unloading is depicted in Fig. 4. The load displacement curves of the unreinforced and TiN reinforced duplex stainless steel are presented in Fig. 5. The load displacement curves exhibited a continuous feature, irrespective of the %wt reinforcement and region of indentation. Instability in plasticity is however not observed. This indicates that the dislocation density beneath the indenter is high with plastic deformation proceeding without nucleation of new dislocations. Consequently, when indents are performed at the ferrite/austenite interface of the TiN reinforced stainless steel, the movement of existing dislocations are restricted and thus pile-up at the interface without dislocation absorption and re-emission in the adjacent boundary [31]. The interaction of dislocations at the interface restricts the penetration of the indenter, thus lowering the penetration depth at the interface. This lower penetration depth with TiN addition is attributed to low energy dissipated in the duplex steels during plastic deformation and the strengthening effect played by the presence of sintered-in nitrides at the ferrite/austenite interface. Generally, the penetration depth in the grains are higher than at the grain boundaries. Pop-in effects were not observed in the loading and unloading curves, this could be attributed to the use of spherical indenter. The stress field beneath a spherical indenter is more diffuse compared with the stress field under a sharp indenter [14,32].

The penetration depths at maximum load (H_{max}) and after unloading (H_f) are determined in accordance with the expressions in equations (1)–(4) and are presented in Table 3. Equations (1) and (2) represents the fitting of the unloading portion of both the grains and grain boundaries with the power function.

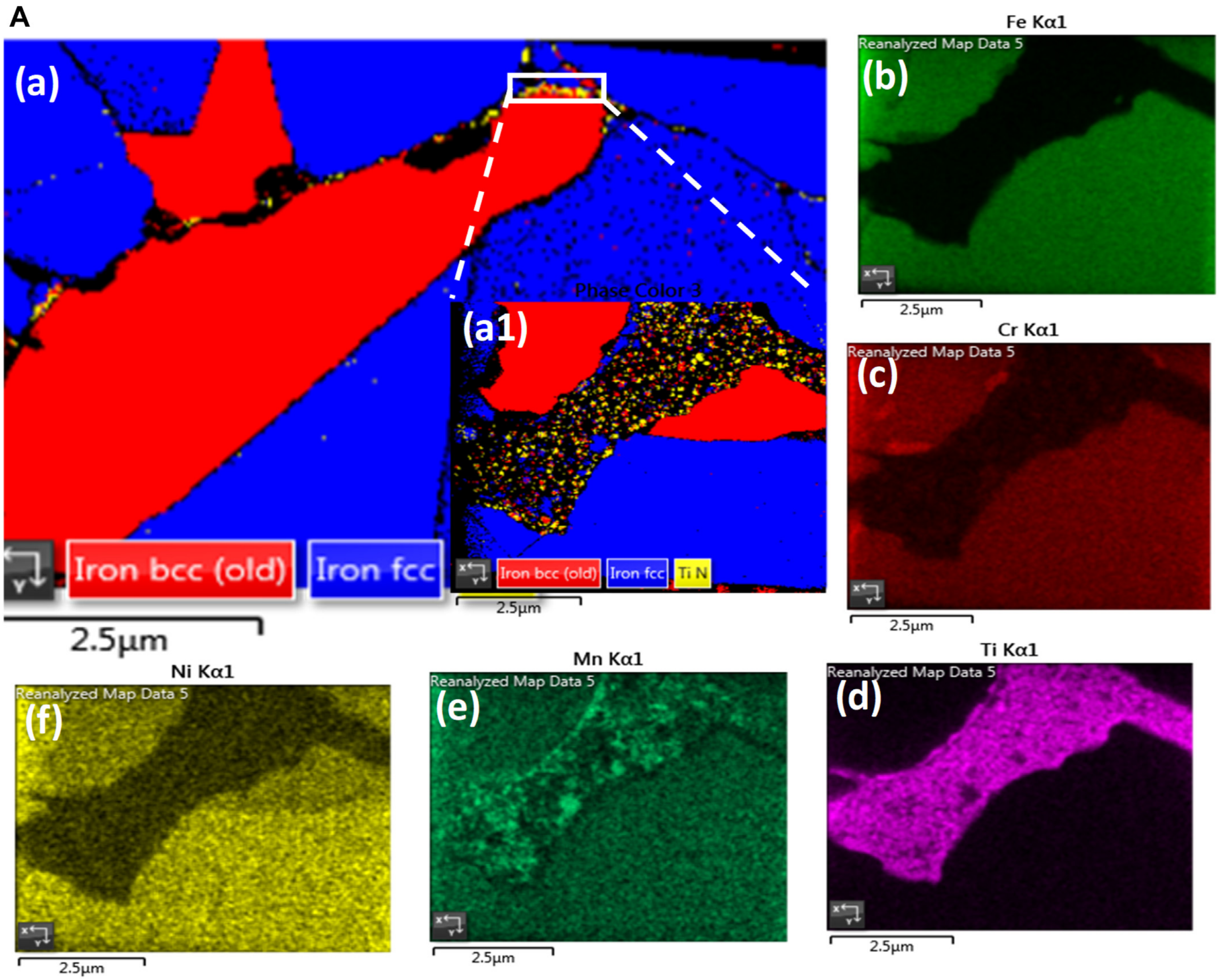

Fig. 3a. Low (a) and high (a1) magnification grain boundary TKD maps of SAF 2205 doped with 4 wt% TiN showing γ-Fe (blue colour), α-Fe (red colour) and TiN (yellow colour). Figs. (b–f): TKD-EDS showing distribution of elements along the grain boundary. (For interpretation of the references to colour in this figure legend, the reader is referred to the Web version of this article.)

$$P = \alpha_1 h^{m_1} \tag{1}$$

$$P = \alpha \left(h - h_f\right)^m \tag{2}$$

where P is the indentation load; h and hf are the instantaneous indenter displacement and final indentation depth respectively; m, α, m_1, α_1 are the empirical fitting parameters. The value of H_{max} can be calculated as expressed in equation (3).

$$h_{max} = h_e + h_c \tag{3}$$

where h_c is the contact depth and h_e is the elastic surface displacement. Using the Sneddon 's solution [33], the contact depth (h_c) can be obtained as written in equation (4).

$$h_c = h_{max} - \varepsilon \frac{P_{max}}{S} \tag{4}$$

where, P_{max} = maximum indentation load; ε is a parameter related to the geometry of indenter and S is the contact stiffness. It is found that the percentage reduction in H_{max} with the addition of 2, 4, 6 and 8 wt% TiN amounts to 42.57, 40.62, 38.78 and 42.25% respectively while that of h_f amounts to 57.63, 57.28, 57.28, 63.59% respectively.

3.2.2. *Hardness and elastic modulus of SAF 2205-TiN nanocomposite*

The loading and unloading curves for both grain and grain boundaries of the reinforced stainless steel are analysed, the reduced elastic modulus (Er) and hardness (H) are estimated using the Oliver-Pharr method [34]. The Er is the collective elastic behaviour of steel samples and the indenter and is expressed as:

$$\frac{1}{Er} = \frac{\left(1 - \vartheta_s{}^2\right)}{E_s} + \frac{\left(1 - \vartheta_i{}^2\right)}{E_i} \tag{5}$$

where ϑ_s and ϑ_i are the Poisson's ratio of the sample and the indenter respectively; E_s and E_i are the elastic modulus of the sample and the indenter respectively. Standardized values of 0.07

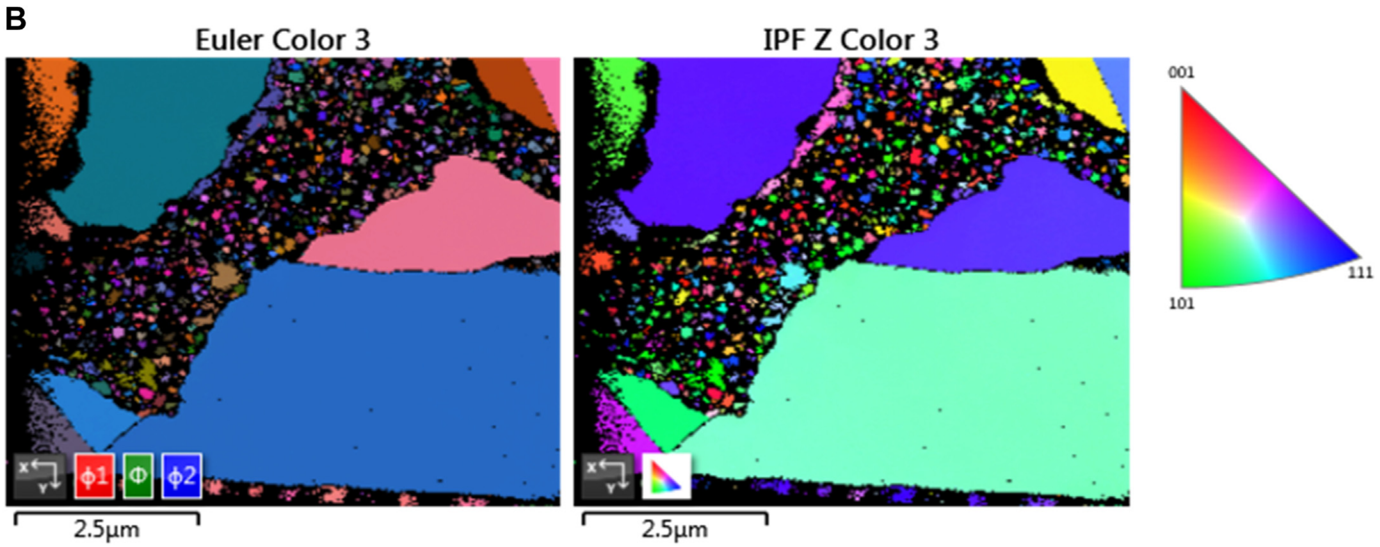

Fig. 3b. Grain boundary Euler and IPF maps of SAF 2205 reinforced with 0 and 4 wt% (S0 and S4) TiN nanoparticles.

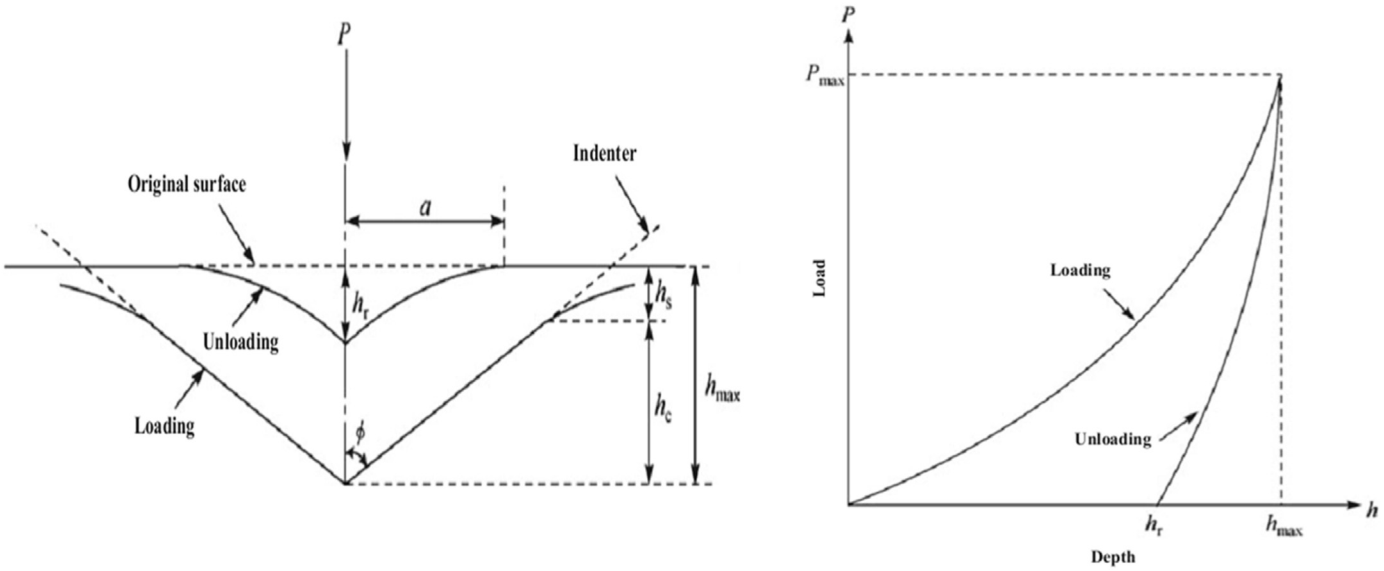

Fig. 4. Characteristic indentation profile and resulting load–displacement curve during loading and unloading.

and 1141 GPa were used in this study as the ϑ_i and E_i of the Berkovich indenter respectively [35]. The ϑ_s of 0.3 for 2205 stainless steel was used while the E_s was obtained from the nanoindentation result data. The grain and grain boundary hardness (H) which measures the resistance of the samples to indentation is expressed as:

$$H = \frac{Pmax}{Ap} \tag{6}$$

P_{max} is the maximum applied load, A_P is the projected area of the indented impression.

The variation in H and Er for grains and grain boundaries with the addition of TiN nanoparticles are presented in Fig. 6. The grain boundaries H and Er are noted to be higher compared to the grains irrespective of the amount of TiN nanoparticle reinforcements. The H and Er at the grain boundaries also increased with the increase in TiN reinforcement from 0 to 8 wt%. Table 4 revealed the percentage increase in H and Er from the grain to grain boundary. The percentage increase in H and Er of the grain to grain boundary ranges from 70.12 to 77.89% and 27.09–39.03% respectively. The increase in H and Er at the ferrite/austenite grain boundary could be linked to the hardening effect of the grain boundary sintered-in nitrides (Fig. 3) and interactions of dislocation during nanoindentation. When indents are made on the grain boundary, plastic strain is initiated and dislocations tend to pile up at the ferrite/austenite interface causing a build-up of stresses under the indenter tip. Soifer et al. [36] reported an increasing trend in hardness in copper when indents are taken close to the grain boundary. The authors attributed the increase in hardness at the grain boundary to thermal pre-history; dislocation-grain boundary interaction; and anisotropy in the slip transfer through the boundary. The increasing trends of the H and Er at the grain boundaries were not observed at the grains. Slight variations in the H and Er values with no specific trend was only noted at the grains. This could be attributed to variations in H and Er properties of the ferrite and austenite phases.

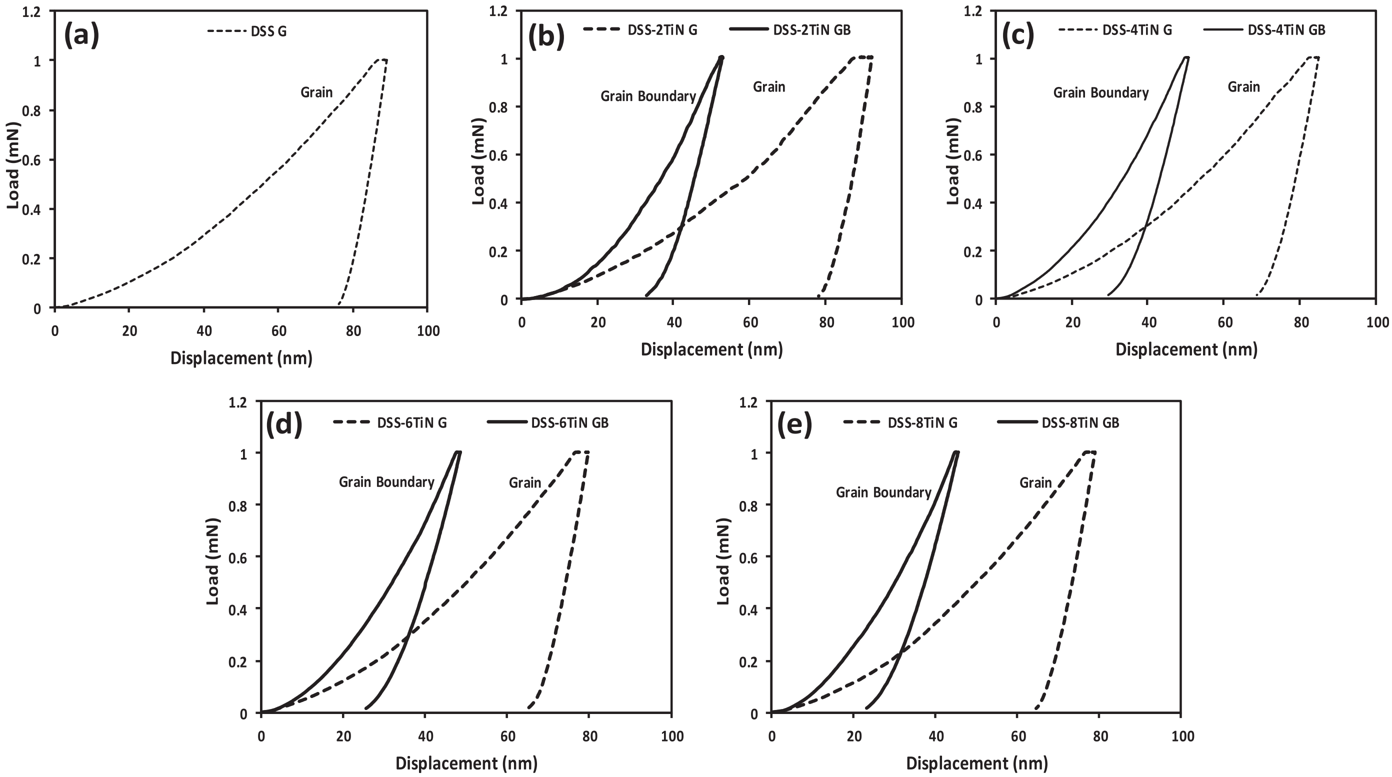

Fig. 5. Nanoindentation load-displacement curves of ferrite/austenite grains and grain boundaries of the SAF 2205 reinforced with (a) 0 (b) 2 (c) 4 (d) 6 (e) 8 wt%TiN nanoparticles.

Table 3
Analysis of indenter penetration depths at grains and grain boundaries derived from the load-displacement curves.

Series	Composite grades	H_{max} Grains (nm)	H_{max} GB (nm)	H_f Grains (nm)	H_f GB (nm)	% [a]Red. depth in H_{max}	% [a]Red. depth in H_f
S0	SAF 2205	88.93	–	76.37	–	–	–
S2	SAF 2205 + 2 wt% TiN	92.08	52.88	78.59	33.3	42.57	57.63
S4	SAF 2205 + 4 wt% TiN	84.93	50.43	69.00	29.48	40.62	57.28
S6	SAF 2205 + 6 wt% TiN	79.81	48.86	65.40	26.01	38.78	60.23
S8	SAF 2205 + 8 wt% TiN	78.93	45.58	64.85	23.61	42.25	63.59

[a] Red. = Reduction.

Variations in ferrite and austenite properties have been reported by Shamanth and Ravishankar [37].

3.2.3. Elastic/plastic behaviour and wear-resistant properties of the SAF 2205-TiN nanocomposite

The elastic-plastic behaviour of the SAF 2204-TiN nanocomposites under stresses and strain were investigated. The irreversible work during nanoindentation (W_p) and the reversible work recovered due to viscoelastic processes during unloading (We) were used to determine the plasticity index (Ψ) of the nanocomposites. The plasticity index ϕ is a parameter that measures the extent to which a material resists plastic deformation under stress, it denotes the quantity of energy that is dissipated in the samples during indentation. Fig. 7a and equation (13) depict the schematic and expression for calculation plasticity index Ψ.

$$\Psi = \frac{Wp}{Wt} \tag{7}$$

where W_t is the total work done by the indenter on the composite during loading and unloading and can be expressed as:

$$W_t = W_e + W_P \tag{8}$$

The results of the calculated plasticity index Ψ values as a function of TiN nanoparticle addition for both the grains and grain boundaries of the stainless steel is presented in Table 5 while the plot of the average plasticity index Ψ is shown in Fig. 7b. Similar trends in the elastic recovery and plasticity index was observed at both grains and grain boundaries. It is evident from the Fig. that the plasticity index Ψ decreased with increase in TiN nanoparticles from 0 to 8 wt%. Higher plasticity index Ψ indicates large plastic deformation, therefore the stainless steel grades reinforced with TiN nanoparticles possess improved resistance to plastic deformation and exhibits enhanced elastic recovery compared to the unreinforced steel. The γ-Fe (FCC) phase has higher hardness compared to the α-Fe (BCC) phase. The plasticity index ϕ at the grain boundaries were noted to be lower than those of the grains. This is obviously due to the role played by the grain boundary nitrides in resisting plastic deformation. Hence, the residual penetration of the indenter in the SAF 2205-TiN composites after nanoindentation is lower at the grain boundaries than the grains. This results to an increase in the nano-hardness.

The calculated mean values of the H and E for the grains and grain boundaries are used to probe the nanocomposite's resistance to wear and plastic deformation. The H/Er ratio have been described as a controlling parameter to a material resistance to wear and elastic

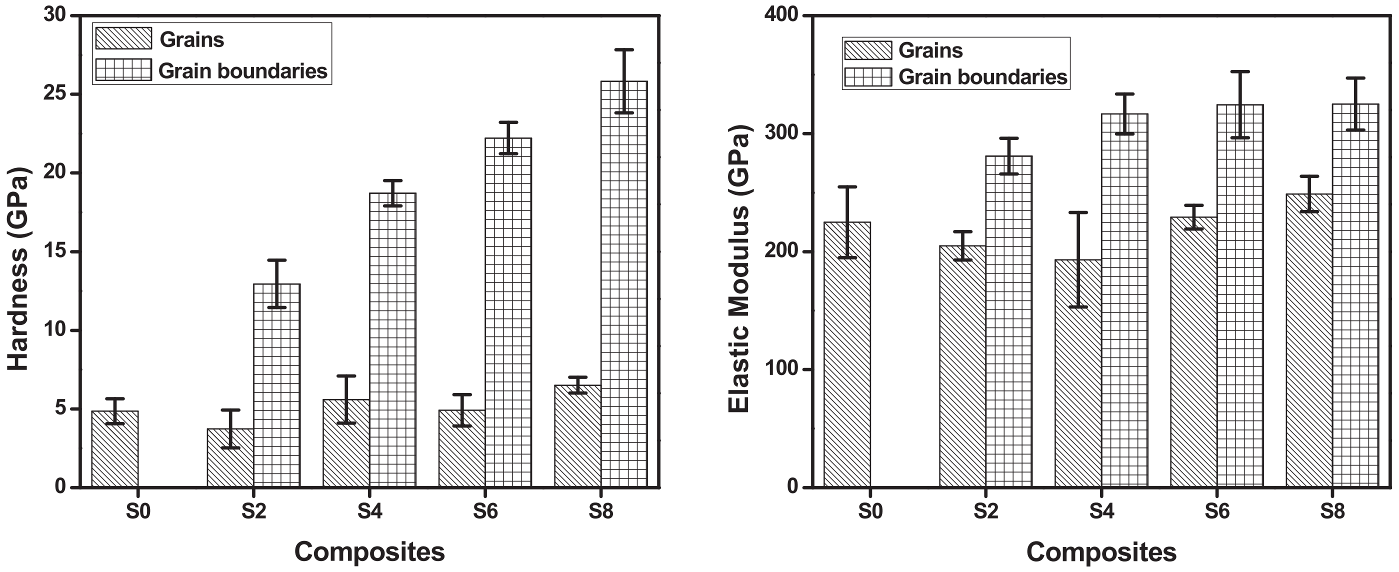

Fig. 6. (a) Variation of grain and grain boundary hardness of the TiN nanoparticles reinforced duplex steel (b) Variation of grain and grain boundary elastic modulus of the TiN nanoparticles reinforced duplex steel.

Table 4
Percentage increase in H and Er from the grain to grain boundary.

Series	Composite grades	% increase in H	% increase in Er
S0	SAF 2205	–	–
S2	SAF 2205 + 2 wt% TiN	71.19	27.09
S4	SAF 2205 + 4 wt% TiN	70.12	39.03
S6	SAF 2205 + 6 wt% TiN	77.89	29.36
S8	SAF 2205 + 8 wt% TiN	74.79	23.43

strain to failure [31]. Another important parameter, H^3/Er^2 (yield pressure) which describes the resistance of a materials to plastic deformation is also estimated. An increase in H/Er and H^3/Er^2 values denotes improved resistance of a material to wear and plastic deformation respectively. Since wear is measured by the degree of material removal which is associated with plastic deformation, the stated parameters can therefore be effectively used to predict the wear resistance of sintered composites. The estimated H/Er and H^3/Er^2 parameters of the TiN nanoparticle reinforced stainless steel is presented in Table 6. It is evident from the plot that the resistance to elastic strain to failure and yield pressure parameters increased with increase in TiN nanoparticle addition from 0 to 8 wt%. This suggests that the TiN reinforced duplex stainless steels show improved resistance to wear and impact loading.

4. Conclusion

Optimized SPS parameters of 1150 °C temperature, 100 °C/min heating rate, 50 MPa pressure and 15 min holding time were utilized for sintering of the SAF 2205 with nanosized TiN reinforcements ranging from 0 to 8 wt%. XRD was used to study evolution of secondary phases, crystallinity and ferrite to austenite transformation of the as-sintered samples. Phase identification and quantification were assessed using EBSD while the ferrite/austenite grain boundary character was studied using TKD. Hardness, Elastic modulus, Elastic/plastic behaviour and wear-resistant properties of the SAF 2205-TiN nanocomposite were evaluated using nanoindentation. The addition of TiN to the SAF 2205 destabilizes the α-Fe phase and promoted α-Fe to γ-Fe transformation with principal planes shifting from α-Fe (110) to γ-Fe (111). The TKD revealed nanosized nitrides concentrated at the grain boundary and coexisted with ferrite and austenite. The load displacement curves exhibited a continuous feature with no evidence of pop-in. The

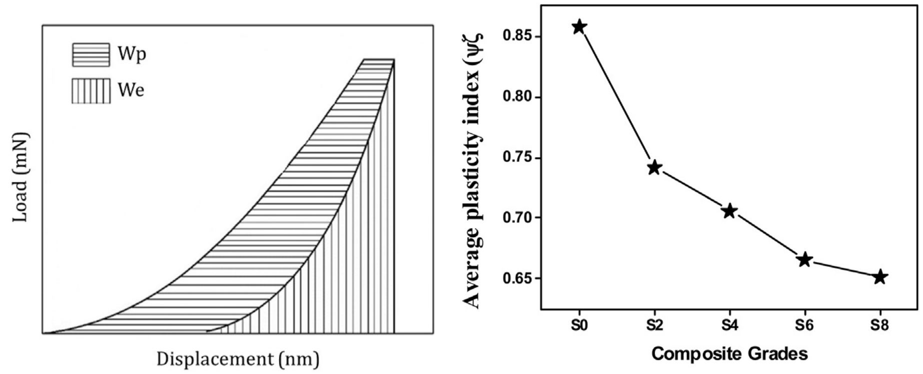

Fig. 7. (a) The load-displacement schematics for evaluating plasticity index (b) the average plasticity index ϕ (grains + grain boundaries) of the SAF 2205-TiN nanocomposite.

Table 5
Calculated values of grains and grain boundaries plasticity index ϕ parameter for the SAF 2205-TiN nanocomposites.

Series	Composite grades	Grains plasticity index Ψ	G. Boundaries plasticity index Ψ	Average plasticity index Ψ
S0	SAF 2205	0.858	–	0.858
S2	SAF 2205 + 2 wt% TiN	0.853	0.630	0.742
S4	SAF 2205 + 4 wt% TiN	0.815	0.596	0.706
S6	SAF 2205 + 6 wt% TiN	0.814	0.518	0.666
S8	SAF 2205 + 8 wt% TiN	0.790	0.511	0.651

Table 6
Estimation of resistance to Elastic Strain to Failure (H/Er) and Yield pressure (H^3/Er^2) of the SAF 2205-TiN using mean values of grain and grain boundary H and Er.

Series	Composite grades	Mean Hardness (GPa)	Mean Elastic Modulus (GPa)	H/Er	Yield pressure (H^3/E^2)
S0	SAF 2205	4.860	224.960	0.022	0.002
S2	SAF 2205 + 2 wt% TiN	10.205	345.335	0.030	0.009
S4	SAF 2205 + 4 wt% TiN	14.945	351.395	0.043	0.027
S6	SAF 2205 + 6 wt% TiN	16.015	391.470	0.041	0.027
S8	SAF 2205 + 8 wt% TiN	19.425	411.405	0.047	0.043

penetration depths at grain boundaries were lower than the penetration depths at the ferrite/austenite grains. The nano-indentation studies showed that the nano-hardness (H), elastic modulus (E), plasticity index ψ, and anti-wear properties were improved at the grain boundaries and with the addition of TiN nanoparticle from 0 to 8 wt%.

Declaration of competing interest

The authors declare that they have no known competing financial interests or personal relationships that could have appeared to influence the work reported in this paper.

CRediT authorship contribution statement

Samuel Ranti Oke: Conceptualization, Data curation, Writing - original draft. **Mahlatse R. Mphahlele:** Methodology. **Oladeji Oluremi Ige:** Supervision, Writing - review & editing. **Oluwasegun Eso Falodun:** Visualization, Investigation. **Avwerosuoghene Moses Okoro:** Formal analysis. **Peter Apata Olubambi:** Supervision.

Acknowledgments

The authors would like to acknowledge the National Research Foundation of South Africa and the Centre for HRTEM, Nelson Mandela University, Port Elizabeth, South Africa for the usage of their facility.

Appendix A. Supplementary data

Supplementary data to this article can be found online at https://doi.org/10.1016/j.jallcom.2020.155648.

Data Availability Statement

The raw/processed data required to reproduce these findings cannot be shared at this time as the data also forms part of an ongoing study.

References

[1] E. Wyszkowska, L. Kurpaska, M. Frelek-Kozak, I. Jozwik, K. Perkowski, J. Jagielski, Investigation of the mechanical properties of ODS steels at high temperatures using nanoindentation technique, Nucl. Instrum. Methods Phys. Res. Sect. B Beam Interact. Mater. Atoms 444 (2019) 107–111.
[2] B.A. Obadele, O.E. Falodun, S.R. Oke, P.A. Olubambi, Spark plasma sintering behaviour of commercially pure titanium micro-alloyed with Ta-Ru, Part. Sci. Technol. 37 (2019) 890–896.
[3] S.R. Oke, O.O. Ige, O.E. Falodun, A.M. Okoro, M.R. Mphahlele, P.A. Olubambi, Powder metallurgy of stainless steels and composites: a review of mechanical alloying and spark plasma sintering, The International Journal of Advanced Manufacturing Technology, 2019.
[4] R. Shashanka, D. Chaira, Effects of nano-Y 2 O 3 and sintering parameters on the fabrication of PM duplex and ferritic stainless steels, Acta Metall. Sin. 29 (2016) 58–71.
[5] C. Tan, C. Wang, S. Wang, G. Wang, L. Ji, Y. Tong, X.-M. Duan, Investigation on 316L/316L-50W/W plate functionally graded materials fabricated by spark plasma sintering, Fusion Eng. Des. 125 (2017) 171–177.
[6] S.R. Oke, O.O. Ige, O.E. Falodun, B.A. Obadele, M.R. Mphahlele, P.A. Olubambi, Influence of sintering process parameters on corrosion and wear behaviour of SAF 2205 reinforced with nano-sized TiN, Mater. Chem. Phys. 206 (2018) 166–173.
[7] O. Ige, S. Oke, M. Mphahlele, S. Aribo, B. Obadele, S. Lephuthing, J. Olawale, O. Ajibola, A. Daniyan, P. Olubambi, Exploring the sintering process parameters on erosion-corrosion characteristics of Fe-Cr-Ni steels in artificial mine water, Tribol. Int. 138 (2019) 79–88.
[8] M. Mphahlele, S. Oke, O. Ige, O. Falodun, P. Olubambi, Effect of TiN nanoparticles on the friction and wear properties of spark plasma sintered Fe-Cr-Ni, Tribol. Ind. (2019) 41.
[9] C. Keller, K. Tabalaiev, G. Marnier, J. Noudem, X. Sauvage, E. Hug, Influence of spark plasma sintering conditions on the sintering and functional properties of an ultra-fine grained 316L stainless steel obtained from ball-milled powder, Mater. Sci. Eng. A 665 (2016) 125–134.
[10] Z. Li, Z. Lu, R. Xie, C. Lu, C. Liu, Effect of spark plasma sintering temperature on microstructure and mechanical properties of 14Cr-ODS ferritic steels, Mater. Sci. Eng. A 660 (2016) 52–60.
[11] S.R. Oke, O.O. Ige, O.E. Falodun, A.M. Okoro, M.R. Mphahlele, P.A. Olubambi, Influence of TiN nanoparticle addition on microstructure and properties of Fe22Cr alloy fabricated by spark plasma sintering, Int. J. Adv. Manuf. Technol. (2019) 1–12.
[12] O. Falodun, B. Obadele, S. Oke, M. Maja, P. Olubambi, Synthesis of Ti-6Al-4V alloy with nano-TiN microstructure via spark plasma sintering technique. IOP Conference Series: Materials Science and Engineering, IOP Publishing, 2017, 012029.
[13] D.E. Spearot, M.D. Sangid, Insights on slip transmission at grain boundaries from atomistic simulations, Curr. Opin. Solid State Mater. Sci. 18 (2014) 188–195.
[14] S.R. Kalidindi, S.J. Vachhani, Mechanical characterization of grain boundaries using nanoindentation, Curr. Opin. Solid State Mater. Sci. 18 (2014) 196–204.
[15] S.J. Vachhani, R.D. Doherty, S.R. Kalidindi, Studies of grain boundary regions in deformed polycrystalline aluminum using spherical nanoindentation, Int. J. Plast. 81 (2016) 87–101.
[16] O.E. Falodun, B.A. Obadele, S.R. Oke, P.A. Olubambi, J. Westraadt, Characterization of spark plasma sintered TiN nanoparticle strengthened titanium alloy using EBSD and TKD, Mater. Res. Bull. 117 (2019) 90–95.
[17] C.F. Dahlberg, J. Faleskog, C.F. Niordson, B.N. Legarth, A deformation mechanism map for polycrystals modeled using strain gradient plasticity and interfaces that slide and separate, Int. J. Plast. 43 (2013) 177–195.
[18] E. Borisenko, D. Borisenko, I. Bdikin, A. Timonina, B. Singh, N. Kolesnikov, Mechanical characteristics of gallium sulfide crystals measured using micro- and nanoindentation, Mater. Sci. Eng. A 757 (2019) 101–106.
[19] M.S. Asl, B. Nayebi, A. Motallebzadeh, M. Shokouhimehr, Nanoindentation and nanostructural characterization of ZrB2–SiC composite doped with graphite nano-flakes, Compos. B Eng. 175 (2019) 107153.
[20] S. Sinha, R. Mirshams, T. Wang, S. Nene, M. Frank, K. Liu, R. Mishra,

Nanoindentation behavior of high entropy alloys with transformation-induced plasticity, Sci. Rep. 9 (2019) 6639.

[21] L. Malekmotiei, A. Samadi-Dooki, G.Z. Voyiadjis, Nanoindentation study of yielding and plasticity of poly (methyl methacrylate), Macromolecules 48 (2015) 5348–5357.

[22] L. Melk, J.J.R. Rovira, F. García-Marro, M.-L. Antti, B. Milsom, M.J. Reece, M. Anglada, Nanoindentation and fracture toughness of nanostructured zirconia/multi-walled carbon nanotube composites, Ceram. Int. 41 (2015) 2453–2461.

[23] M.E. Maja, O.E. Falodun, B.A. Obadele, S.R. Oke, P.A. Olubambi, Nanoindentation studies on TiN nanoceramic reinforced Ti–6Al–4V matrix composite, Ceram. Int. 44 (2018) 4419–4425.

[24] S.J. Vachhani, S.R. Kalidindi, Grain-scale measurement of slip resistances in aluminum polycrystals using spherical nanoindentation, Acta Mater. 90 (2015) 27–36.

[25] X. Li, B. Bhushan, A review of nanoindentation continuous stiffness measurement technique and its applications, Mater. Char. 48 (2002) 11–36.

[26] S.R. Oke, O.O. Ige, O.E. Falodun, P.A. Olubambi, J. Westraadt, Densification and grain boundary nitrides in spark plasma sintered SAF 2205-TiN composite, Int. J. Refract. Metals Hard Mater. 81 (2019) 78–84.

[27] S.R. Oke, O.O. Ige, O.E. Falodun, B.A. Obadele, M.B. Shongwe, P.A. Olubambi, Optimization of process parameters for spark plasma sintering of nano structured SAF 2205 composite, J. Mater. Res. Technol. 7 (2018) 126–134.

[28] S. Oke, O. Ige, O. Falodun, M.R. Mphahlele, P. Olubambi, Densification behavior of spark plasma sintered duplex stainless steel reinforced with TiN nanoparticles. IOP Conference Series: Materials Science and Engineering, IOP Publishing, 2018, 012034.

[29] J. Simmons, Overview: high-nitrogen alloying of stainless steels, Mater. Sci. Eng. A 207 (1996) 159–169.

[30] J.-Y. Maetz, T. Douillard, S. Cazottes, C. Verdu, X. Kleber, M23C6 carbides and Cr2N nitrides in aged duplex stainless steel: a SEM, TEM and FIB tomography investigation, Micron 84 (2016) 43–53.

[31] A.M. Okoro, R. Machaka, S.S. Lephuthing, S.R. Oke, M.A. Awotunde, P.A. Olubambi, Nanoindentation studies of the mechanical behaviours of spark plasma sintered multiwall carbon nanotubes reinforced Ti6Al4V nanocomposites, Mater. Sci. Eng. A 765 (2019) 138320.

[32] S. Pathak, J. Michler, K. Wasmer, S.R. Kalidindi, Studying grain boundary regions in polycrystalline materials using spherical nano-indentation and orientation imaging microscopy, J. Mater. Sci. 47 (2012) 815–823.

[33] I.N. Sneddon, The relation between load and penetration in the axisymmetric Boussinesq problem for a punch of arbitrary profile, Int. J. Eng. Sci. 3 (1965) 47–57.

[34] W.C. Oliver, G.M. Pharr, An improved technique for determining hardness and elastic modulus using load and displacement sensing indentation experiments, J. Mater. Res. 7 (1992) 1564–1583.

[35] S.-R. Jian, G.-J. Chen, T.-C. Lin, Berkovich nanoindentation on AlN thin films, Nanoscale Res. Lett. 5 (2010) 935–940.

[36] Y.M. Soifer, A. Verdyan, M. Kazakevich, E. Rabkin, Nanohardness of copper in the vicinity of grain boundaries, Scripta Mater. 47 (2002) 799–804.

[37] V. Shamanth, K. Ravishankar, Dissolution of alpha-prime precipitates in thermally embrittled S2205-duplex steels during reversion-heat treatment, Results Phys. 5 (2015) 297–303.